Preprint typeset in JINST style - HYPER VERSION

Performances of a LYSO crystals prototype of Electromagnetic Calorimeter

SuperB EMC Group

ABSTRACT: The high luminosity of the SuperB experiment requires an electromagnetic calorimeter in the forward region which should be able to operate under high rates. In order to test the potentialities of a calorimeter made of LYSO crystals a prototype has been assembled and tested on a beam of electrons, protons and pions at the CERN SPS experimental area

Contents

1. Introduction

SuperB is a proposed new effort to study e^+e^- collisions in the region around $b\bar{b}$ threshold at a much higher luminosity (10^{36} cm^{-2}s^{-1}) than presently available [3, 2, 1]. The detector for this will reuse several of the components of the BaBar detector. However, higher luminosity implies higher rates and higher backgrounds, so it is not possible to simply reuse the entire detector. One of the components that need to be replaced is the forward electromagnetic calorimeter (EMC), which provides energy and direction measurement of electrons and photons, as well as contributes to particle identification. We report here on test beam studies of a new design for the forward EMC, using LYSO(Ce) crystals.

The present BaBar calorimeter is based entirely on CsI(Tl) crystals, each with two PIN photodiodes for detection of the scintillator light. However, in the forward region, from $\cos\theta = 0.896$ to 0.965, where θ is the angle with respect to the higher energy beam, these crystals will no longer meet the requirements. The decay time of CsI(Tl) (680 ns and 3.4 μs) is too slow for the high rates expected in this region, and CsI(Tl) is not sufficiently radiation hard. A promising candidate for

the forward EMC, with high light output, fast response (40 ns), and radiation hardness, is cerium-doped LYSO (lutetium-yttrium oxyorthosilicate). LYSO also has a shorter radiation length (1.14 cm) compared with CsI (1.85 cm), and a smaller Molière radius (2.1 vs 3.6 cm), implying a thinner device and better position resolution with smaller transverse crystal dimensions.

We are thus proposing to construct a forward EMC for SuperB based on LYSO. Fig. **?? MISSING FIGURE** illustrates the concept. Present design is for 20 rings of crystals. These rings are subdivided into four groups of five rings each. Each group is segmented into modules five crystals wide. The number of crystals in a group ranges from 900 to 1050, for a total of 4500 crystals. The number of modules in each a group is a multiple of six, permitting the detector to be split into two halves if this is deemed necessary for installation.

A nearly projective geometry is chosen, hence the crystals are tapered with trapezoidal cross section. Each crystal is 2.5×2.5 cm^2 at the back end. This is both a reasonable match to the Molière radius and permits two crystals to be cut from a single boule. In order to adequately contain showers up to several GeV, the crystals are 20 cm in lenght, or 17.5 X_0.

An alveolar structure, with a "cell" for each crystal, is being investigated for the mechanical support. This would be constructed from either carbon or glass fibers. At the outer and inner radii of the calorimeter, support would be provided by conical structures. The outer radius is at the boundary with the barrel calorimeter (re-used from BaBar), so must be thin in radiation lengths. This may be accomplished with 6-10 mm of carbon fiber. No such requirement exists for the inner cone, and a relatively thick aluminum cone can be used. Different options are being investigated for the front (towards the interaction point) support, which will include a source calibration system similar to BaBar's, and possibly cooling loops. The entire forward EMC is supported from the back with a stainless steel structure.

The choice of readout is constrained by the need to operate in a strong magnetic field produced by the detector solenoid. While PIN diodes were used in BaBar, APDs (avalanche photodiodes) provide attractive advantages, most notably low-noise amplification. At a gain of 50, it is possible to use sub-MeV radioactive sources to prepare the crystals, including adjusting the light collection uniformity along the length of the crystal. To improve light collection, to provide a back-up in case of device failure, and to provide redundant information useful in recognizing the nuclear counter effect from neutron background, there will be two APDs on each crystal. The APD gain is strongly temperature-dependent (a few per cent/degree, dependent on bias), so good monitoring of the temperature is important, as well as maintaining good short-term stability.

For the test beam, we assembled a prototype calorimeter. A 5×5 array of full-sized, tapered LYSO(Ce) crystals is used, with additional CsI(Tl), on loan from the CLEO detector, around the sides to provide for leakage detection. A prototype alveolar constructed from glass fiber holds the LYSO crystals. Readout is with either APDs or PIN diodes. The test beam runs were performed at the 1-3 GeV region at CERN, and the 100-500 MeV region at Frascati. Further details of the prototype and the test beam are given in following sections.

2. Description of prototype

Crystals (including lab-measurements) (CalTech)

Mechanics (PG)

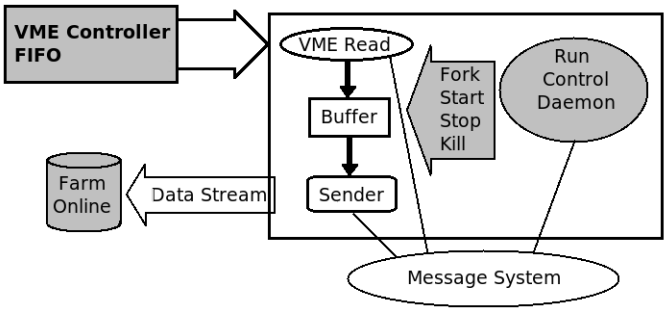

Figure 1. Schematics of the test beam data acquisition.

Detectors and Electronics (including power supplies)(RM1)

3. Description of test setup

We test took place at the T10 beam line at CERN. Its nominal momentum resolution is 0.24%. We could select particles whose energy spanned from 1 to 6 GeV. The spill lasted 400 ms and the duty cycle of the beam was variable from 1-4%. Particle flux during the spill could vary from a few hundred to several thousands. The measured electron content of the beam spanned from 60% at 1 GeV to 1% at 6 GeV.

In addition to reading the crystals that constitute the prototype as described in Sec. 2 we have utilized two external detectors: a Cherenkov detector capable of discriminating between electrons and hadrons with negligible contamination and a scintillating pad located behind the crystal matrix to detect particles leaking from the rear.

The trigger was asserted by a coincidence of scintillators on the beam line. The Cherenkov signal was used to down scale pions thus enriching the sample in electrons. After each trigger a variable dead time was inserted via an IO register in order to let the DAQ process read all the event fragments.

The read-out chain is based on VME bus. A Motorola MVME6100 VME Processor is responsible for the complete read-out system. The schematic view of the system architecture is shown in Fig. 1

During data acquisition the software reads data from the VMEbus controller and sends them via Gigabit-Ethernet to the online farm that consists of a PC equipped with two Intel Xeon (TM) CPUs running at 3.06GHz with HiperThreading and a 512 kB cache each with a total of 4GB RAM. The MVME6100 CPU has a 100/1000 Ethernet interface connected by UTP cat. 5e cable to a 100/1000 switch. The on-line farm CPU is also the boot server of the front-end CPU.

The information delivered from the LYSO matrix was converted by four Caen V1720 flash ADCs. The CsI (Tl) crystals readout, the environmental system parameters, and the Cherenkov signals are digitized by a Caen V785 ADC. Finally, the silicon telescope is read-out via a Caen V550 and a Sequencer. An event-building procedure has been implemented at crate level.

The farm software in principle could perform event-building by collecting streams of data delivered from several different CPUs housed in different VME crates. The front end boards can be read both in single access and in BLT. The software process (collector) reads data from the front

end FIFOs and delivers them in a circular buffer [9] **WHICH REFERENCE IS THIS?** which is read by another process (sender). The sender sends them via Gigabit-Ethernet to the on-line farm using a TCP/IP protocol. A receiver process collects data at the farm level through a TCP/IP socket. The data are delivered onto a circular buffer read by another process which is in charge of performing event-building and storing them on a disk. The system bandwidth was limited by silicon telescope read-out to about 100 Hz. To speed up the read-out we have implemented a zero suppression procedure. In this way the silicon strip whose recorded signal was compatible with their noise were not read.

The on-line processes are distributed on several nodes in the data acquisition network. It is therefore necessary for them to communicate by means of an efficient message passing system. All processes have to change their state in a coherent way, following a local or remote command. The message passing system was largely inspired by the one already used in the KLOE experiment. The structure of a typical data acquisition process, and its interaction with the message system, are described in the following. At the startup, the process specifies a set of its more significant variables, in order to subscribe to a ÔÔprocess tableÕÕ, implemented as a UNIX shared memory. A process message queue is created and its identification is also saved in the table. During the process activity, the value of its variables is periodically updated. All the commands are distributed delivering a software interrupt to the process and a string which contains the command to execute. The process which receives the command executes it and adjourns a variable in a shared memory. The process which delivers the command can therefore check that variable and understand whether the command was executed or not. The average completion time for a command is about 1 ms mainly due to TCP/IP protocol latency. To deliver command and manage the run we have also developed a Graphical User Interface (GUI) written in Java language.

4. Description of Simulation (PG)

Effects included

Expected breakdown of contributions on electrons

5. 5. Selection of events (PG)

5.1 MIPS

5.2 Electrons

6. Noise studies

The noise of each crystal i is analyzed in the Fourier space, by estimating its power spectrum from waveforms acquired with a random trigger:

$$\mathrm{PS}_i(\omega_k) = < n_i(\omega_k) n_i^*(\omega_k) > \tag{6.1}$$

where ω_k is the k-th component of the discrete Fourier transform (DFT) of a noise waveform, and $<>$ denotes the average taken over a large number of waveforms. We recall that the quantity that

contributes to the energy resolution is the noise fluctuation in the time domain ($\sigma_i^{\rm noise}$), which can be expressed in terms of Eq. 6.1 as:

$$\sigma_i^{\rm noise} = \sqrt{\sum_k {\rm PS}_i(\omega_k)}\,. \tag{6.2}$$

Estimated power spectra of four representative crystals are shown in Fig. 2, where it can be seen that the dominant source of noise is in the range 0-8 MHz, which corresponds to the frequency bandwidth of the shaper. Sources of noise occurring after the shaper give a negligible contribution, while those occurring before are filtered according to the shaper transfer function and dominate. The noise fluctuation $\sigma_{\rm noise}$ was found to be, averaged over all channels, 2.1 ADC counts, with a dispersion max-min equal to 0.3 ADC counts. Crystal 18 was the only outlier with $\sigma_{\rm noise} = 3.3$ ADC counts.

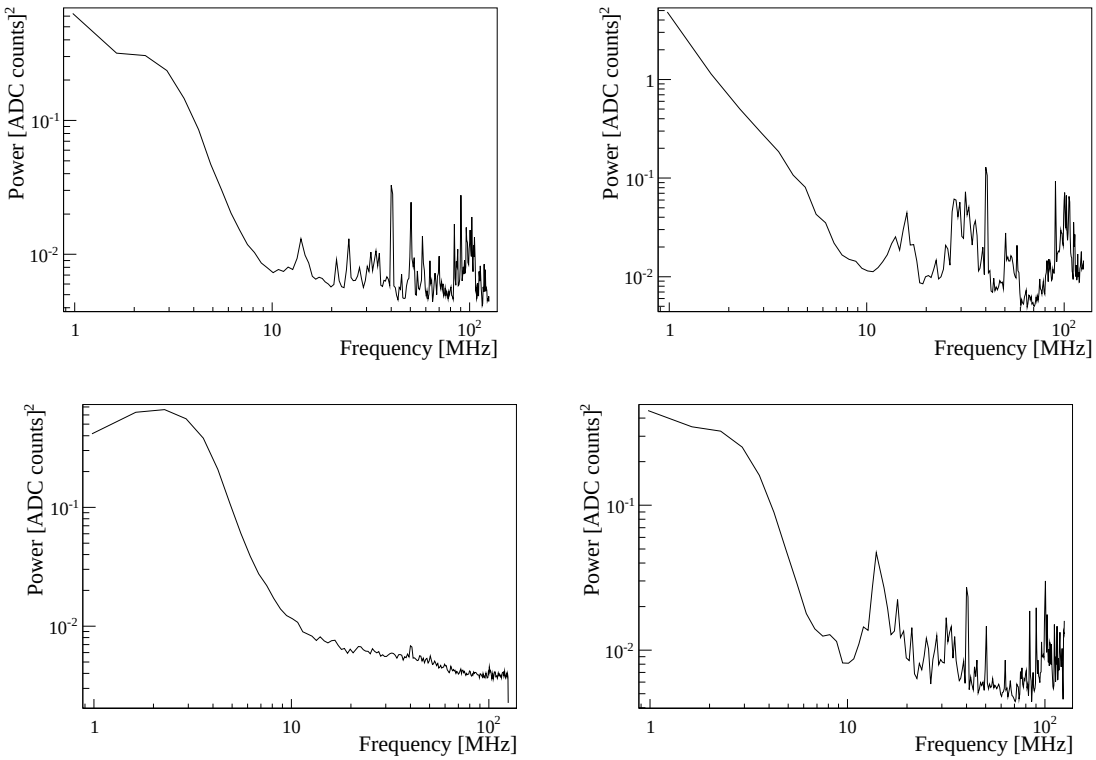

Figure 2. Noise power spectrum measured on crystals 10 (top left), 18 (top right), 12 (bottom left) and 2 (bottom right).

We investigated the presence of a possible correlation between the noise observed on different crystals. The correlation can be in principle present, because the APDs in the matrix are biased by a unique power supply, and each Front End board serves 5 crystals **VB: CHECK THIS PLEASE!**. If the noise is found to be correlated, it would point to a common source of noise that hopefully can be identified and removed.

The covariance between crystals i and j has been estimated as

$$\mathrm{COV}_{ij}(\omega_k) = < n_i(\omega_k) n_j^*(\omega_k) > \tag{6.3}$$

where the definitions are the same as in Eq. 6.1. The magnitude of an element of these matrices is the covariance between two crystals as usually intended in the real domain, while the phase is the relative time delay between them. As a consequence the correlation is also a complex quantity, which is defined as:

$$\rho_{ij}(\omega_k) = \frac{\mathrm{COV}_{ij}(\omega_k)}{\sqrt{\mathrm{PS}_i(\omega_k)\mathrm{PS}_j(\omega_k)}} \,. \tag{6.4}$$

The two crystals with the highest correlation below 8 MHz were number 2 and 10, and the corresponding plot is shown in Fig. 3. It can be seen that the correlation is, on average, very small in the region of interest. Fig. 4 summarized the correlation matrix averaged in the ranges 0-8 MHz, 8-40 MHz and 40-125 MHz. The plots indicate that the noise correlation is negligible, and that each crystal has an independent noise source.

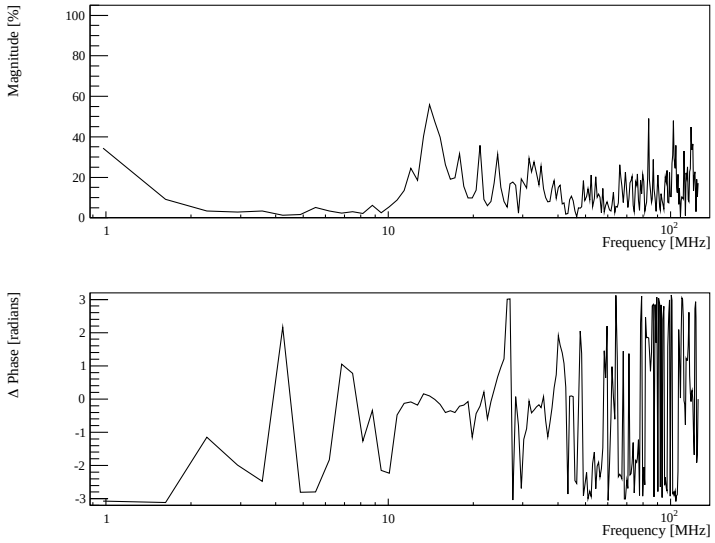

Figure 3. Correlation between crystals 2 and 10 as a function of the frequency. The phase takes random values when the magnitude is zero, when this happens its value should not be considered.

Comments on HV stability
PIN-APD comparison

7. 7. Studies on MIPs

Charged hadrons release in a significant fraction of cases a known amount of energy in a single crystal and this makes this sample particularly suited to intercalibrate the crystals and to study corrections to the energy measurement. The criteria described in Sec. 5.1 select events where the charged hadrons release their energy exclusively by ionization in a single crystal. Such events are therefore labelled as minimum ionizing particles (MIP). The raw energy of a MIP is the energy measured in the only crystal with significant energy. When performing studies with this sample we will call "energy" the raw energy multiplied by a factor that matches the mean value in data with the expectation from simulation.

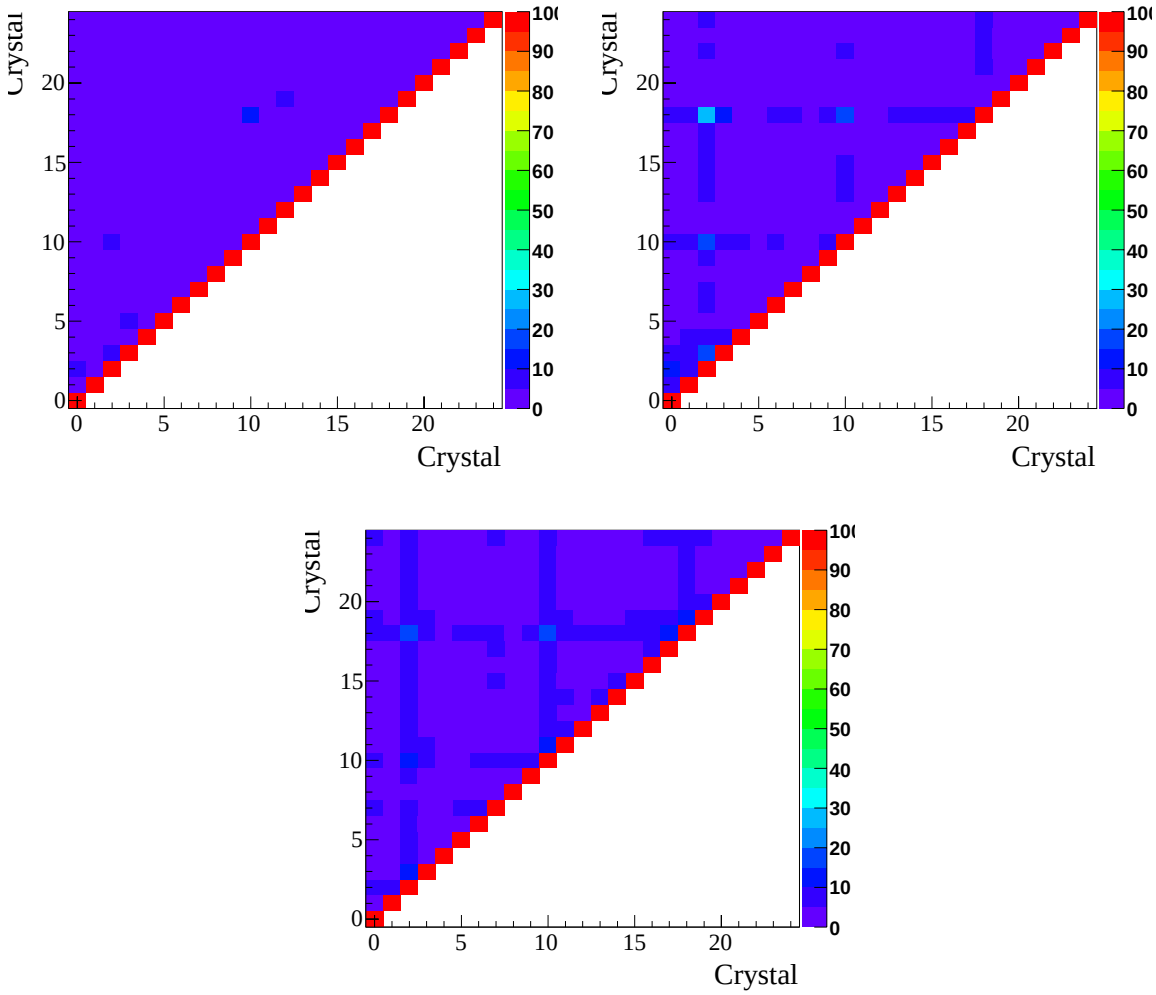

Figure 4. Noise average correlation in different frequency bandwidths, 0-8 MHz (top left), 8-40 MHz and 40-125 MHz.

7.1 Data-MC comparison

The detailed simulation described in Sec. 4 has been used to estimate the expected MIP energy energy spectrum. Since the beam could potentially contain both protons and pions with the same momentum, both were considered. Their energy spectrum, shown in Fig. 5 in the case of $p =$ 1GeV, reveals that pions and protons are significantly different. The relative RMS (mean) of the distributions for pions and protons are 6.3% (240 MeV) and 5.4% (460 MeV) respectively. The spread in the measured energy is dominated by fluctuations in the energy loss and therefore this sample cannot be used for resolution studies.

The distribution of the energy released in the MIPs sample after selection in the high gain configuration is compared with MC expectations in Fig. 6. There is good agreement bettwen the distrubutions under the hypothesis that only pions are present in the sample.

The comparison between the energy measured in the case of high and low gain after normalization to the same energy scale (Fig. 7)and after releasing the constraint on the pad behind the

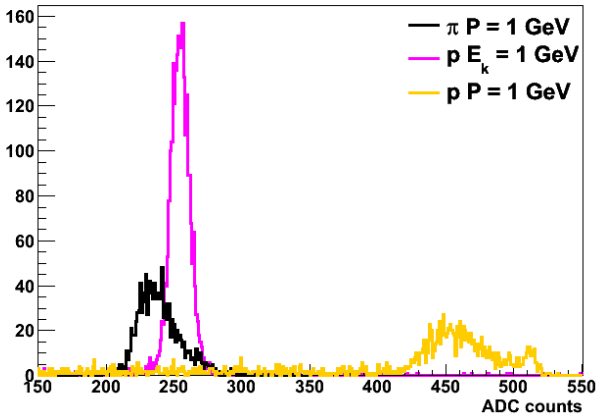

Figure 5. MC simulation of the energy released by MIPs in the high gain configuration.

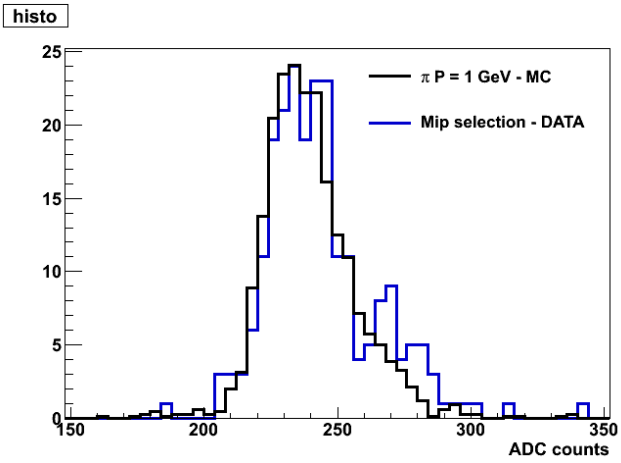

Figure 6. Comparison between data and MC under the pion hypothesis of the energy deposited in the MIPs sample.

crystal matrix shows that the spread is comparable, thus confirming that it is dominated by fluctuations in the energy release. It also shows that the pedestal widths scale with the gain and that therefore the source of the noise is upstream of the amplifier. **REVIEW ARGUMENT**

7.2 Temperature correction

A temperature dependence of several percent per degree is expected both in the light yield of the LYSO crystals and in the gain of the APDs. The position of the MIP peak as a function of the temperature measured by the sensors (Fig. 8) has been used to extract the temperature correction:

$$E_{corr} = E_{raw}/(1 - p_0 * (T - T_0)) \tag{7.1}$$

where $p_0 = 2.8 \pm 0.2 \times 10^{-3}$ and $T_0 = 34$K. The same figure shows also the effect of the correction.

WHERE ARE THE SENSORS DESCRIBED?

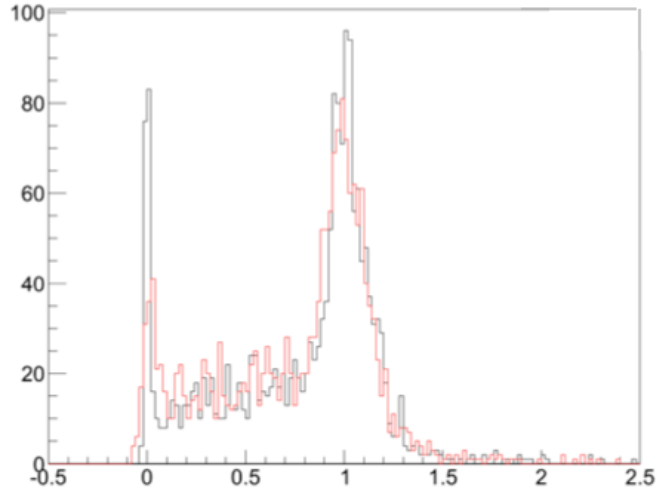

Figure 7. Comparison between the distributions of the measured energy separately in the low gain (red) and high gain (black) samples. The energy scales are normalize to enforce the peak at the value of 1.

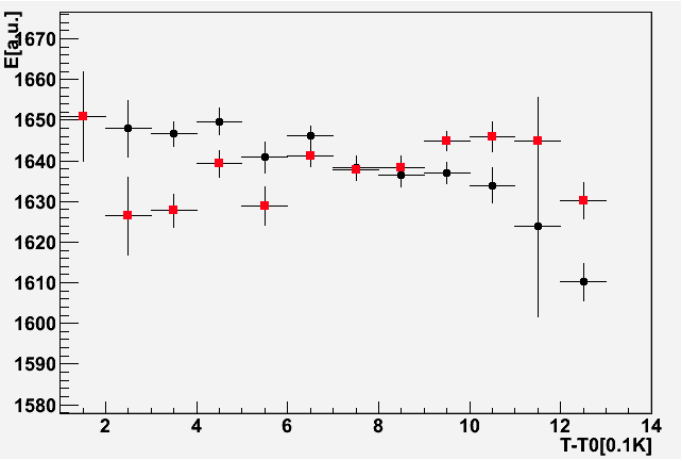

Figure 8. Dependence of the measured energy on the temperature before (black dots) and after (red squares) correction.

Figure 9. Energy distribution of a MIP with the fit to a Landau convoluted with a gaussian superimposed.

7.3 Intercalibration

Since MIPS release their energy in just one crystal they are an ideal sample to intercalibrate crystals. To this aim several runs were taken moving the crystal matrix in such a way that each crystal in turn has been shot by the beam in the middle. The mean value of the deposited energies should be the same modulus the fact that each crystal presented a different angle with respect to the beam line. Corrections for this effect were calculated with MC simulation and revealed to be negligible. The distributions of the deposited energies after temperature correction were fitted with the convolution of a landau distribution and a gaussian resolution(see Fig. 9). The intercalibration constant of a crystal were estimated by dividing the mean value of the deposit in the central crystal (#12) by the

Table 1. Intercalibration constants estimated with MIPS. The matrix represents the crystal matrix and the numbers in square brackets is the corresponding crystal id.

[0]2.106±0.024	[1]2.058± 0.017	[2]2.972±0.017	[3] 2.59±0.04	[4] 2.18±0.04
[5]1.263±0.008	[6] 1.085±0.004	[7] 0.5379±0.003	[8] 1.131±0.005	[9] 0.979±0.012
[10]1.757±0.012	[11] 0.886±0.004	[12] 1.000±0.003	[13] 1.029±0.006	[14] 0.965±0.008
[15]1.265±0.014	[16] 1.148±0.008	[17] 1.220±0.010	[18] 2.178±0.015	[19] 1.178±0.012
[20]0.629±0.005	[21] 1.134±0.009	[22] 1.133±0.011	[23] 1.075±0.007	[24] 1.165±0.011

corresponding mean value in the crystal itself. The measured constants are summarized in Tab. 1.

8. Studies on electrons (PG)

Energy measurement

Intercalibration procedures (and estimate of error?)
Temperature corrections
Linearity for both gains Ð we should include also the MIPs point
Resolution for both gains Ð MIPs and electronic noise included?
Comparison with simulation

9. Conclusions

References

[1] M.E. Biagini. SuperB Progress Reports: The Collider. 2010. Long author list - awaiting processing.

[2] E. Grauges et al. SuperB Progress Reports – Detector. 2010.

[3] B. O'Leary et al. SuperB Progress Reports – Physics. 2010.